https://doi.org/10.26599/FRICT.2026.9441311

Research Article

Design of pearl shell-inspired biomimetic textured rollers and their tribological performance during roller hemming

Xiyu Zhang [a], Liwu Miao [c], Ziqiang Zhang [d], Hongwei Zhao [a,e,f], Jianwei Sun [g], Juntao Guo [h], Changyi Liu [a,b]*, Tianye Yang [a]*

a National Key Laboratory of Automotive Chassis Integration and Bionics/ School of Mechanical and Aerospace Engineering, Jilin University, Changchun 130025, China

b Key Laboratory of Bionic Engineering, Ministry of Education, Jilin University, Changchun 130025, China

c Inner Mongolia First Machinery Group Co. LTD, BaoTou 014000, China

d Changchun University of Science and Technology, Ministry of Education Key Laboratory for Cross-Scale Micro and Nano Manufacturing, Changchun 130000, China

e Institute of Structured and Architected Materials, Liaoning Academy of Materials, Shenyang 110167, China

f School of Mechanical and Electrical Engineering, China University of Mining and Technology, Xuzhou 221116, China

g School of Mechatronic Engineering, Changchun University of Technology, Changchun, 130012, China

h National Key Laboratory of Science and Technology on Advanced Composites in Special

Environments, Harbin Institute of Technology, Harbin 150080, China

Correspondence

Changyi Liu, Professor, Key Laboratory of Bionic Engineering, Ministry of Education, Jilin University, Changchun 130025, P. R. China.

E-mail address of the corresponding author: liuchangyi@jlu.edu.cn.

Tianye Yang, Professor, National Key Laboratory of Automotive Chassis Integration and Bionics/ School of Mechanical and Aerospace Engineering, Jilin University, Changchun, 130025, China.

E-mail address of the corresponding author: yangty@jlu.edu.cn.

Received: March 11, 2026; Revised: August 3, 2026; Accepted: September 2, 2026

Abstract

The wear condition of the roller surface on the roll-forming end effector significantly affects the quality of automotive body molds and the service life of the corresponding equipment. To address these issues, this study proposes a biomimetic roller design strategy based on the microstructure of the pearl shell surface. A corresponding texture-morphology mapping model was established, followed by multi-scale mechanical and tribological performance analysis. Simulation results indicate that, under the same depth-to-width ratio conditions, the roller with arcuate grooves exhibits the lowest friction energy loss and the highest principal stress compared to rollers with vertical and rhombic grooves. Friction wear tests further validate the advantages of this structure, showing significantly lower coefficients of friction, wear depth, and wear mass than those of rollers with vertical and rhombic textures, demonstrating superior wear resistance. Based on this, the depth-to-width ratio structure of the arcuate striped roller was further optimized using the golden section method, determines a global optimal depth-to-width ratio of 0.775. Compared to ordinary rollers, the maximum principal stress along the rolling direction increased by 18.3% for the optimized roller, while rolling friction energy decreased by 70.28%. This study demonstrates that biomimetic textures can significantly improve the surface stress distribution and tribological performance of rollers, provide theoretical support and innovative solutions for enhancing the stability of automotive body manufacturing processes and the reliability of intelligent devices.

1. Introduction

The roller hemming process is extensively employed in the edge forming of automotive components such as doors and engine hoods. The friction and wear behavior of the rollers significantly influences the precision and surface quality of the workpieces [1]. In practical applications, severe wear on the roller surfaces not only degrades the forming quality but may also lead to defects such as scratches, thereby increasing scrap rates and economic losses [2]. Consequently, enhancing the wear resistance of roller surfaces has become a critical technical issue for improving the efficiency and quality of hemming operations.

To address these friction and wear issues, various surface wear resistance technologies have been proposed [3], including the selection of hard alloy materials [4-6], surface coatings [7-8], thermal treatments, and the design of biomimetic textures [9-10]. In recent years, biomimetic surface texture technology [11-12] has garnered significant interest, as it does not rely on high-hardness materials while effectively reducing friction and enhancing wear resistance under complex conditions. This approach involves emulating the micro-nano structural features of natural biological surfaces to construct micro-textured units with functional gradients or adjustable geometric characteristics on material surfaces [13]. Such modifications result in a significant enhancement of tribological performance in dry friction environments [14-16], under lubrication [17-19], and in alternating load conditions [20-22]. Existing studies have demonstrated the promising application potential of biomimetic textures in reducing friction and enhancing wear resistance on engineering surfaces. For instance, Tong et al. [23] designed a biomimetic roller mimicking the abdominal structure of dung beetles, achieving a 25% reduction in wear mass. Zhao et al. [24] employed leaf vein-like textures to enhance the wear resistance of thrust bearing surfaces. Johannes et al. [25] effectively reduced the friction coefficient of bearing steel through the application of snake-scale-like textures. These findings demonstrate the prospective application of biomimetically textured surfaces in the control of tribological interfaces.

From a micro-mechanical perspective, the influence of different surface textures on tribological behavior is mediated by mechanisms such as the regulation of lubricant film formation [26], reduction of actual contact area [27], and the entrapment of wear debris [28]. Research conducted by Babu [29] and Arslan [30] indicates that when the depth-to-width ratio of dimples lies between 0.2 and 0.5, with a surface coverage density of 10%–30%, there is an enhancement in the microfluid dynamic pressure effect, which reduces the coefficient of friction to 55% of that of an untreated surface. Kovalchenko [31] and Uehara [32] observed that when the depth of dimples exceeds 15 μm, their capacity to capture wear debris is significantly enhanced, contributing to a wear rate reduction by up to 60%. Additionally, directional groove structures exhibit superior lubrication performance; Wakuda [33] and Chilamakuri [34] found that with a depth-to-width ratio of 0.3-0.6 and an inclination angle of 30°-60°, these grooves can guide the flow of lubricant, thereby enhancing film stability. Ren et al. [35] further validated the advantages of these structures under boundary lubrication conditions. The study of surface evolution in nature into biomimetic textures provides a source of inspiration. The shell of the marine organism, the pearl oyster, with its regular ridged structures on the exterior and a stacked porous lamellar structure internally, exhibits not only excellent erosion resistance but significantly improved fatigue strength and wear resistance, serving as a theoretical model for the construction of high-performance engineering surfaces. To overcome the limitations of existing roller structures characterized by poor wear resistance and inadequate fatigue performance under extreme conditions, it is crucial to pursue in-depth research on biomimetic roller texture designs based on the multiscale composite structures of pearl shells. Such research is essential for achieving highly durable, fatigue-resistant, and stable high-performance surfaces in roller hemming engineering applications.

Previous studies have shown that the tribological benefits of textured surfaces arise not only from their geometric morphology but also from their functional mechanisms. Surface textures can serve as lubricant reservoirs, promote local hydrodynamic pressure generation, and redistribute contact stresses, thereby reducing friction, wear, and rolling contact fatigue under rolling–sliding conditions [36–40]. Since roller hemming involves repeated rolling–sliding contact under high contact pressure, these mechanisms are expected to contribute to improved tribological performance. Inspired by the rib-like texture on pearl shell surfaces, our previous work demonstrated that a biomimetic textured hemming roller exhibited enhanced wear resistance during roller hemming operations [41], providing the basis for the present study.

In this biomimetic design, the unique surface morphology of the pearl shell is transformed into an engineered roller texture design, rather than traditional grooves. As shown in Figure 2(a), pearl shells have a layered growth ridge structure and an ordered surface architecture. Its geometric organization can effectively transmit stress and improve the damage resistance of the working surface [42,43].

Based on these biometric features, three typical texture geometries were developed. The arcuate texture is derived from the arc-shaped growth ridges of pearl shells and abstracts the continuous curvature of biological structures to achieve smoother contact transitions and reduce local stress concentrations during rolling deformation [42]. Vertical texture is inspired by the directional arrangement of shell surface structures and has anisotropic load transfer characteristics, which can improve contact stability under cyclic mechanical loads [43]. The design of the rhombic texture is based on the interconnected and staggered structural characteristics of mother-of-pearl. This nested structure helps achieve multi-directional stress redistribution and enhances mechanical integrity [44]. Therefore, the proposed texture is a structural transformation of the pearl shell morphology into a functional engineered surface rather than arbitrary grooves introduced simply to increase surface roughness [41]. Inspired by the aforementioned insights, this study utilizes the ridged structure of the pearl oyster shell surface as a biomimetic prototype to design a biomimetic roller with striped microstructures. Through systematic analysis using the finite element method, this study examines the stress distribution and frictional response of the biomimetic roller during the hemming process and, by integrating single-factor comparative tests, investigates the impact of the shape, size, and depth-to-width ratio of biomimetic units on the wear resistance of the roller. The results demonstrate that appropriately configured biomimetic textures significantly mitigate wear rate, enhance tool life, and improve forming quality. This research provides a theoretical foundation for the optimized design and industrial application of biomimetic rollers, with significant prospects for extending the life of critical components, reducing maintenance costs, and finding applications in fields such as construction machinery and rail transport.

2. Experimental Procedures

2.1. Structural Design Methodology

The LT850 five-axis laser texturing machine tool (Haitian Optics, China) was employed for manufacturing biomimetic roller surfaces with textured patterns. The LT850 is equipped with a five-axis coordinated motion system, delivering dynamic precision of 0.005 mm, capable of high-precision machining of complex surfaces. The laser operates at a wavelength of 1053 nm with a maximum power output of 1 kW. Fig. 2(a) illustrates the design principle of the biomimetic textured rollers. Initially, the textural parameters of the biomimetic roller were derived from the biological surface mapping of the pearl oyster shell. Fig. 2(b)-(d) display the biotexture characteristics of the pearl oyster shell surface captured using the Keyence V7000 microscope. By integrating the operational principles of the roller hemming end-effector, the design and development of biomimetic roller samples with arcuate, vertical, and rhombic textures were undertaken. These were compared against ordinary rollers with smooth surfaces. Supplementary Table S1 lists the specific parameters of the textured surfaces.

2.2 Material Characterization

Post-friction samples were obtained from friction and wear experiments. These samples were sectioned into blocks along the X-Y plane using an electrical discharge machining tool and were secured using fixtures. The surface micro-wear features of the textured roller samples, exhibiting arcuate, vertical, and rhombic structures, were analyzed using a scanning electron microscope (SEM, JSM-IT500A, JEOL, Japan) and a confocal microscope (LEXT OLS4100, Japan). SEM settings for morphological observation included an acceleration voltage of 10 kV and a working distance of 10 mm. The biomimetic roller samples were further studied for microsurface wear characteristics using a confocal microscope (LEXT OLS4100, Japan) with a Z-axis resolution of 0.01 μm.

2.3 Mechanical Performance Simulation

Biomimetic textured roller samples were divided into four groups: vertical stripes, arcuate stripes, rhombic stripes, and ordinary rollers. The depth-to-width ratios for the vertical, arcuate, and rhombic rollers were respectively designated as 0.50, 0.67, 0.80, 0.86, and 0.89. The mechanical and tribological performances were simulated using Abaqus software, focusing on the maximum principal stress and frictional energy under normal pressure conditions. The feed rate for the rollers was set at 100 mm/s.

2.4 Wear Testing and Analysis

In this study, roller samples characterized by biomimetic textures were selected as the tribological pair. Prior to the friction and wear testing, the roller samples were sectioned into blocks measuring 10×10×3 mm. These samples underwent wire cutting followed by degreasing and derusting treatments. Subsequently, their surfaces were polished to facilitate the measurement of the friction coefficient. The measurements were conducted on a multifunctional friction and wear tester (SRV5, Germany) employing reciprocating friction and wear tests. A 100CR6 bearing steel ball with a diameter of 6 mm was chosen as the counterbody in this study. The friction motion parameters were set as follows: a stroke of 1 mm, a frequency of 40 Hz, and a sliding duration of 1800 seconds.

Following the friction coefficient tests, a reciprocating friction test rig for rollers, as depicted in Fig. 1, was designed and constructed to analyze the wear quality and depth of the rollers. The specific motion involved the rollers reciprocating along the feed direction, thereby generating friction against the plate. This study focused on the final edge rolling process with the rolling operation divided into two steps: initially, the plate angle was set at 30 °before edge rolling, and subsequently adjusted to 0 °post-edge rolling to achieve a folded configuration. The wear depth and quality were measured using a high-precision vernier caliper and a high-precision electronic scale, with accuracies of 0.001 mm and 0.0001 g, respectively. A scanning electron microscope (SEM, JSM-IT500A) was utilized to investigate the microstructural wear characteristics of the roller surfaces at different hierarchical levels. The SEM settings were adjusted to an acceleration voltage of 10 kV and a working distance of 10 mm. A confocal microscope was employed to collect micro-frictional characteristics along the fear surface direction, aiming to study the influence of texture parameters and shapes on the tribological properties of the roller surfaces.

The reciprocating friction and wear tests of this study were conducted under dry friction laboratory conditions to ensure experimental repeatability. In actual automobile roller hemming, the contact interface may retain lubricants, oxide films, surface contaminants and be affected by environmental conditions. These factors will change the contact and lubrication state, thereby affecting the absolute values of friction coefficient and wear rate. However, the dominant contact mechanism of roller hemming is still repeated rolling-sliding action under contact pressure, so the experimental results are mainly suitable for evaluating the relative advantages and disadvantages of different texture geometries in reducing friction and improving wear resistance. The wear values in this article are comparative indicators under controlled conditions, and their engineering reference value is reflected in the screening and sorting of texture schemes, rather than absolute life prediction in actual service environments.

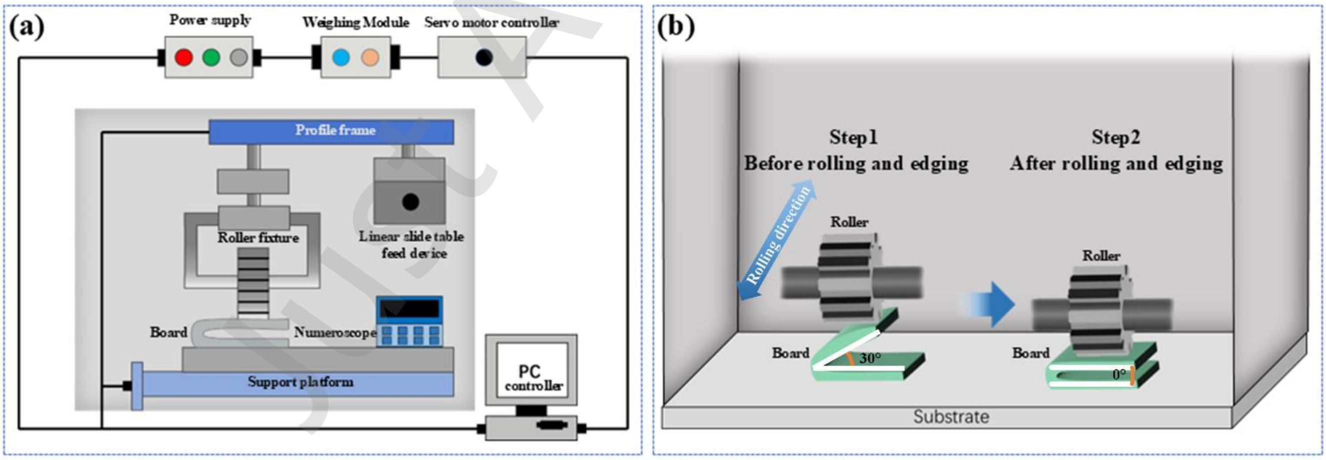

Fig. 1 Reciprocating friction test rig for rollers: (a) reciprocating friction test rig for rollers, (b) detailed view of the contact configuration.

The reciprocating sliding wear method was employed to measure the friction coefficients, wear quality, and depth of rollers with varying texture shapes and depth-to-width ratios, to explore the effect of these texture parameters on the roller's wear resistance. The reciprocating motion was aligned with the direction of plate rolling, and the rollers were subjected to 10,000 reciprocating cycles at a constant feed rate. The multifunctional friction and wear tester (SRV5, Germany) and the reciprocating friction test rig for rollers were used to conduct the on-plate rolling sliding reciprocating wear tests at room temperature. To ensure the reliability and reproducibility of the experimental data, each test was repeated three times under the identical conditions.

2.5 Correlation between stress distribution, frictional energy dissipation and wear behavior

In this study, there is a clear coupling relationship among the maximum principal stress, rolling friction energy and wear behavior. The maximum principal stress mainly reflects the load transmission capacity and local load-bearing characteristics of the roller structure during the contact process, while the rolling friction energy characterizes the degree of energy dissipation at the contact interface. Higher load transfer efficiency can reduce random slippage and ineffective friction at the contact interface, thereby lowering energy loss during the rolling process.

For biomimetic textured rollers, periodic surface structures can reconstruct the contact load path, concentrating contact stress more effectively within stable load-bearing regions while reducing unstable contact behavior at the interface. As a result, although local areas exhibit higher maximum principal stresses, overall friction energy is reduced, indicating that load transfer at the contact interface becomes more stable and efficient. The reduction in friction energy further suppresses continuous plastic deformation and abrasive wear processes on the material surface, thereby minimize material delamination and wear accumulation. This observation shows good consistency with both simulated wear depth results and experimental wear mass data. Notably, the roller with arcuate grooves and a depth-to-width ratio of 0.775 not only exhibits the lowest friction energy but achieves the smallest wear depth and wear mass, demonstrating a clear synergistic relationship among stress optimization, reduced energy dissipation, and enhanced wear resistance.

3. Results and Discussion

3.1 Design of the Biomimetic Roller and Wear-Resistant Test Rig Structure

Fig. 2(a) presents a schematic of the roller hemming robot’s operating principles. Supplementary Material Figure S2 also depicts the operational mechanics of the roller hemming robot. During its operation, the user adjusts the motion trajectory through the control system, enabling the roller hemming robot to follow a specified path for roller hemming tasks, thus completing the hemming process. Based on the actual working conditions of the equipment and the specific parameters of the roller, the outer and inner diameters of the roller are set at 60 mm and 50 mm, respectively. The roller material is DC04 steel, which is characterized by its high wear resistance, good toughness, and relatively soft texture. Not only is this material extensively used in tensile testing and cold roll forming, but also it is predominantly utilized in the manufacturing of automotive body panels, as indicated by its material properties in Table S2.

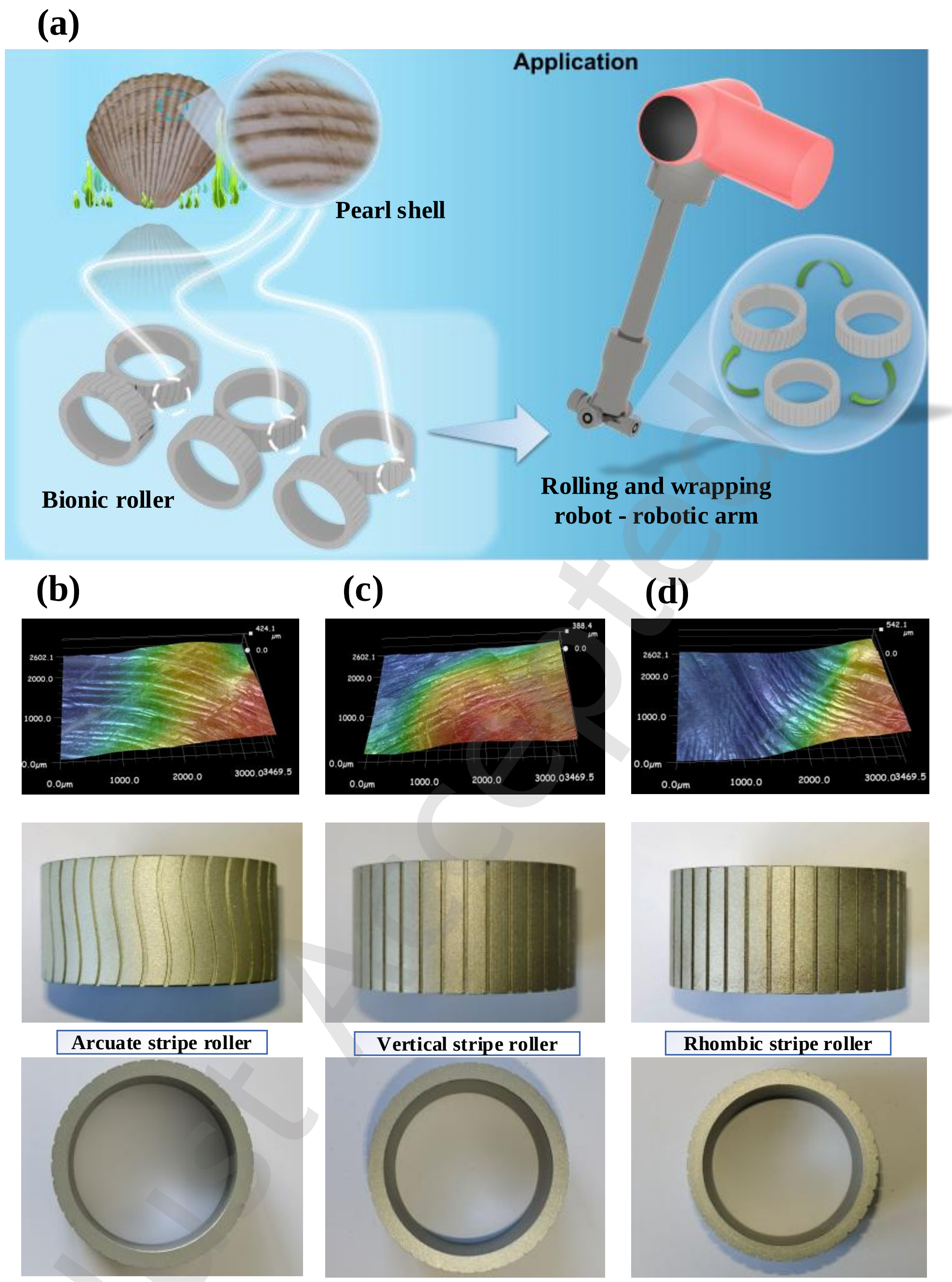

Fig. 2 Operational principle and structural design diagram of the roller hemming robot: (a) biomimetic inspiration and application, (b) arcuate stripe roller, (c) vertical stripe roller, (d) rhombic stripe roller.

As depicted in Fig. 2(b) to 2(d), the design integrates the textural structure of pearl oyster shells with the actual specifications of the roller, resulting in three types of biomimetic rollers featuring arcuate, vertical, and rhombic stripes. The structural parameters of these biomimetic striped rollers are detailed in Supplementary Material Table S1 and Figure S2. Figure S2(a) shows the main and top views of the roller with arcuate stripes, where the arcuate pattern is arranged in an intersecting arc formation, with an outer diameter of 60 mm and an inner diameter of 50 mm. The waveform is represented as y=sin12t, and the stripes are spaced 10 °apart, totaling 36 stripes. Figure S2(b) illustrates the main and top views of the roller with vertical stripes, where the texture is uniformly distributed in a cylindrical form, the radius of the roller is 30 mm, and the outer contour of the texture is linearly distributed as y=t, with the cross-section appearing rectangular. Each texture is spaced

10 ° apart, totaling 36 stripes, with the roller's inner diameter being 50 mm and the outer diameter 60 mm. Supplementary Material Figure S2(c) presents the front and top views of a roller featuring rhombic stripes. These rhombic textures are uniformly distributed in an oblong cylindrical arrangement around the circumference of the roller, which has an inner diameter of 50 mm and an outer diameter of 60 mm. The texture profile linearly varies with the equation y=t, and the cross-sectional view displays a parallelogram distribution. Each texture is spaced 10 ° apart, with an inclination angle of 35 °, totaling 36 textures along the circumferential surface direction. The roller sample was fabricated using a laser marking machine, employing DC04 steel for the roller structure. Figures S3-S5 in the Supplementary Material depict samples of rollers with arcuate, vertical, and rhombic stripes. Figures S3-S5 (a) - (e) display top views of biomimetic rollers with depth-to-width ratios of 0.50, 0.67, 0.80, 0.86, and 0.89, respectively. Figures S3-S5 (f) - (j) show the front views of rollers with arcuate stripes at the same depth-to-width ratios. The details of the stripes are illustrated in Supplementary Material Figures S3-S5 (h). Considering the structural characteristics of the roller wear testing rig and the operational mechanism of the roller during the roller hemming process, a reciprocating friction test rig was designed, as shown in Fig. 1. The structure of this test rig primarily consists of a linear slide, roller clamping device, mechanical sensors, a 485 module, a stepper motor, a stepper motor driver, a stepper motor controller, and a profile frame assembly.

3.2 Experimental Analysis of Friction and Wear in Biomimetic Rollers

By conducting experiments on the friction and wear behavior of biomimetic rollers, the study reveals the tribological performance optimization mechanism afforded by biomimetic textures on the surface of the roller. This investigation provides a basis for adapting the parameters of surface textures for actual operating conditions and enhancing the long-term wear resistance of the rollers.

It is worth noting that none of the roller samples are intentionally subjected to black oxidation treatment, and all samples underwent identical processing and cleaning procedures to maintain consistent surface conditions. This ensures that any differences in the tribological performance of the roller samples are unrelated to oxidation treatments and are entirely attributable to the designed surface textures.

In order to further analyze the elemental composition of the roller surface and whether there is a transfer film during the wear process, EDS surface scanning analysis was performed on arcuate, vertical and rhombic texture rollers with a depth-to-width ratio of 0.5 after the rolling hemming test, as shown in Figure S8. Among them, Figure S8(a), Figure S8(b) and Figure S8(c) respectively show the EDS analysis results of the texture area of the arcuate, vertical and rhombic texture rollers, with the detection area size is 1.00mm × 1.00mm; Figure S8(a_1), Figure S8(b_1) and Figure S8(c_1) respectively show the EDS analysis results of the non-texture area indicated by the corresponding arrows, and the detection area size is 100.00μm × 100.00μm.

Among them, the EDS analysis results show that the textured and non-textured areas of the three rollers are dominated by Fe element, and their mass fractions remain above 97 wt.%, indicating that the roller matrix still remains exposed. Except for Fe element, only a small amount of O, Mn, Si, S and P elements were detected in each detection area. Among them, the content of Mn, Si, S and P elements changed little, and there was no obvious enrichment phenomenon between each area, indicating that no obvious element migration or composition change occurred on the surface of the roller during the rolling and hemming process. Compared with the non-texture area, the O element content in the three texture areas increased. Among them, the O element mass fraction in the arcuate texture area increased from 0.4 wt.% to 1.4 wt.%, the vertical texture area increased from 0.4 wt.% to 1.3 wt.%, and the rhombic texture area increased from 0.5 wt.% to 1.3 wt.%, which is 2.6-3.5 times that of the corresponding non-texture area. This shows that during the repeated rolling-sliding contact process, textured pits are more likely to retain oxygen-containing wear products, causing local oxygen enrichment in the textured area.

It is worth pointing out that although the O element content in the texture area has increased relatively, its overall content is still low, and Fe element has always been absolutely dominant, and no new element enrichment has been detected that is obviously different from the composition of the roller matrix. Therefore, the EDS results prove that there is no continuous transfer film or oxidation film formed on the surface of the roller, and no pre-oxidation treatment characteristics are found on the surface of the roller. Combined with the EDS results, it can be concluded that the texture area only has local retention of oxidized wear debris or oxygen-containing wear products during the wear process, rather than forming an oxide layer or transfer film that continuously covers the surface of the roller.

It should also be noted that the friction test employs ball-plane contact, which is a point contact configuration, whereas in practical applications, the contact is typically between a roller and a flat plate, representing a line contact. Under dry friction conditions, both configurations follow Amonton's law, meaning the steady-state coefficient of friction is proportional to the normal load and independent of the nominal contact area. Friction behavior primarily depends on material pairs, surface roughness, and sliding velocity, rather than macroscopic curvature of the contacting bodies. Therefore, the friction coefficients obtained from ball-plane contact tests can be directly applied to roller-on-flat conditions, and differences in contact geometry do not affect the conclusions of this study.

3.2.1 Testing of Friction Coefficient for Biomimetic Rollers

For undertaking a simulation analysis of biomimetic rollers, it is necessary to ascertain their friction coefficients. The method for determining these coefficients is as follows: initially, the roller is sectioned into slices. These slices are then subjected to a reciprocating friction test using a micro-motion friction testing machine. The measurement process involves dry friction under high-frequency motion, during which friction and wear behavior is observed on the surfaces of the tribological pair. The friction motion parameters were set as follows: a stroke of 1 mm, a frequency of 40 Hz, and a sliding duration of 1800 seconds. The test is conducted with a material density of 7800 kg/m^3 over a duration of 30 minutes. Fig. 3 illustrates the friction coefficients of rollers with arcuate, vertical, and rhombic stripes. The mean values of these coefficients are available in Supplementary Table S6. Under identical depth-to-width ratios, rollers with arcuate stripes exhibit the lowest friction coefficients, followed by rollers with rhombic and vertical stripes. Ordinary rollers show the highest friction coefficients. For rollers with arcuate stripes, the friction coefficient ranges between 0.5738 and 0.6202. When the depth-to-width ratio is between 0.5 and 0.80, there is a positive correlation between the friction coefficient and the depth-to-width ratio. Between depth-to-width ratios of 0.80 and 0.89, the friction coefficient firstly decreases and then increases, reaching its minimum value at a depth-to-width ratio of 0.86, showing a reduction of 34.57% compared to ordinary rollers. Beyond a depth-to-width ratio of 0.86, the friction coefficient once again shows a positive correlation with increasing depth-to-width ratio, indicating that 0.86 is the critical point for optimal friction coefficient in rollers with arcuate stripes. For rollers with vertical stripes, within the depth-to-width ratio range of 0.5 to 0.80, the friction coefficient correlates positively with depth-to-width ratio and reaches its minimum at a depth-to-width ratio of 0.50, showing a reduction of 28.16% compared to ordinary rollers. As the depth-to-width ratio increases from 0.80 to 0.89, the frictional coefficient exhibits a decreasing and then increasing trend. For rollers with rhombic stripes, a similar pattern is observed, where within the depth-to-width ratio range from 0.5 to 0.80, the frictional coefficient correlates positively with depth-to-width ratio. As the depth-to-width ratio increases from 0.80 to 0.89, the friction coefficient decreases and then increases, reaching its minimum value at a depth-to-width ratio of 0.86, showing a reduction of 29.30% compared to ordinary rollers. Thus, a depth-to-width ratio of 0.86 is identified as the critical point for optimal friction coefficient in rollers with rhombic stripes. The friction coefficient will be used for the preprocessing settings of the simulation analysis.

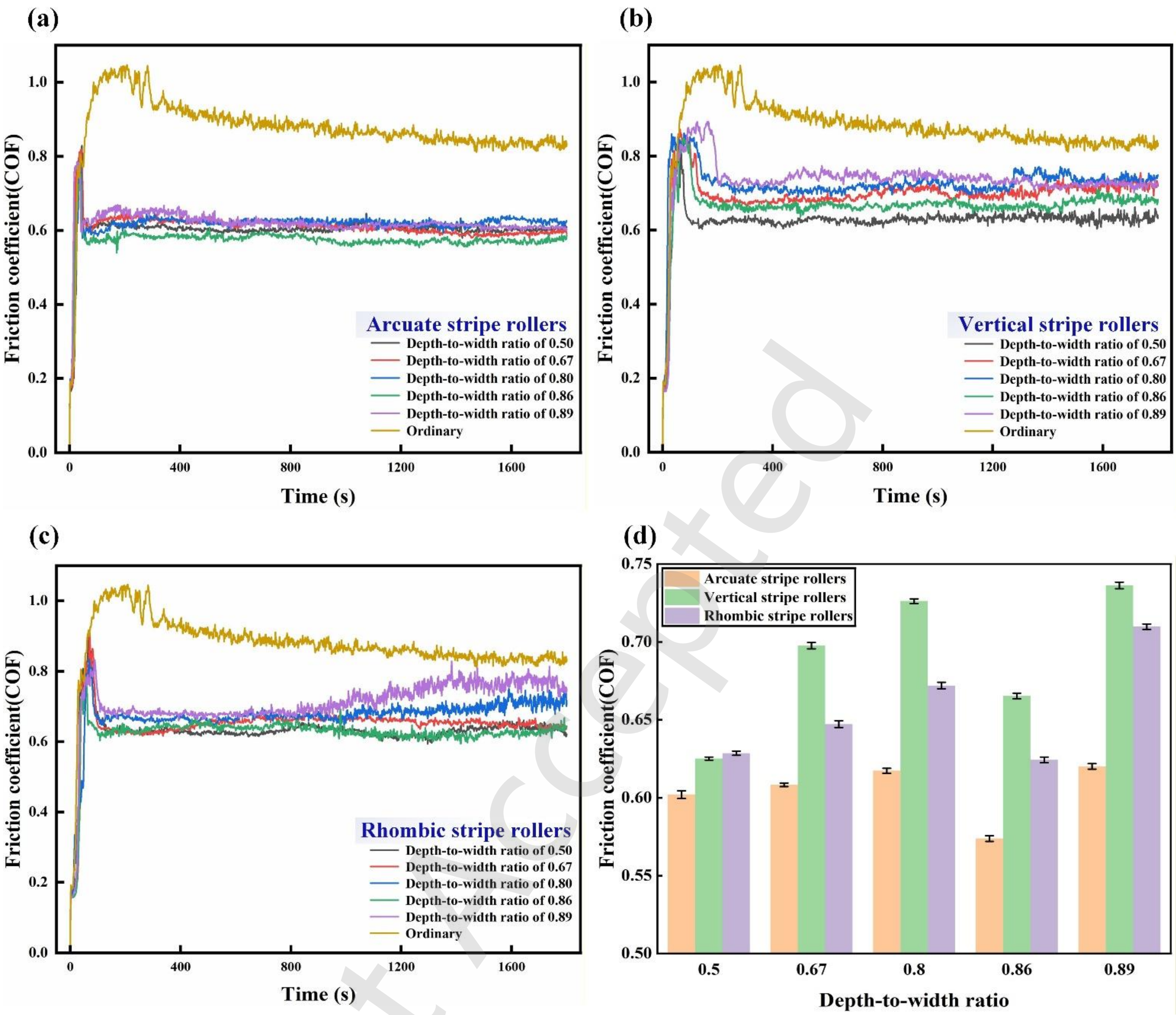

Fig. 3 Evolution of friction coefficient with sliding time for biomimetic rollers: (a) arcuate stripe rollers, (b) vertical stripe rollers, (c) rhombic stripe rollers, (d) comparison of average friction coefficients at different depth-to-width ratios.

The observed variation in friction coefficient in Figure 3 can be attributed to the synergistic effect of surface texture on contact mechanics and debris dynamics under dry reciprocating motion conditions. Among them, the friction coefficient of the arc-shaped stripes is the lowest, ranging from 0.5738 to 0.6202. This is due to its curved geometry, which can minimize stress concentration at the texture edges and provide a continuous debris capture path, thereby reducing abrasive friction. Compared to the ordinary roller with a smooth surface, the vertical stripes, although reducing by 28.16% at a depth-to-width ratio of 0.50, have a higher overall friction coefficient because their straight edges induce local shear stress peaks, thereby increasing adhesion. Compared to the ordinary roller with a smooth surface, the rhombic stripes reduce by 29.30% at a depth-to-width ratio of 0.86, achieving balance by forming closed pockets, effectively capturing worn debris, but increasing shear resistance at the contact angle. With changes in the depth-to-width ratio, the arc-shaped stripes reach a minimum value at a depth-to-width ratio of 0.86, reducing by 34.57% compared to the ordinary roller with a smooth surface, presenting a non-monotonic trend, which reflects that a depth-to-width ratio less than 0.5 is insufficient to store debris, causing abrasive particles to remain at the interface; while for a depth-to-width ratio greater than 0.86, it will cause the raised platform to bear excessive normal load, thereby increasing local pressure and adhesion. For the arc-shaped and rhombic stripe rollers, the optimal depth-to-width ratio is 0.86, which maximizes the debris retention without weakening the load-bearing capacity, achieving the minimum friction. As shown in Table S6, after optimizing the aspect ratio using the golden section method, the friction coefficient of the arcuate stripe roller was the lowest, ranging from 0.5516 to 0.5710, and the wear resistance was significantly improved. Moreover, when the aspect ratio was 0.7750, the friction coefficient reached the minimum value of 0.5516.

3.2.2 Biomimetic Roller Friction and Wear Testing

To comprehensively evaluate the overall performance of biomimetic textures under actual operational conditions, we expanded upon the foundational friction coefficient experiments by quantifying the cumulative damage evolution through wear quality and depth tests. This approach concurrently elucidates the synergistic mechanism between the friction-reducing properties and the long-term wear resistance of the biomimetic roller surface. The experiments were conducted using a reciprocating friction test rig (depicted in Fig. 1), aiming to systematically assess the wear resistance of the roller. Evaluative metrics included wear quality, wear depth, and standard deviation, which primarily characterize the anti-wear capabilities of the roller under specified experimental conditions, with standard deviation serving to measure the dispersion and stability of the wear quality and depth data.

The expressions for wear quality (Δm) and wear depth (Δh) are given as follows:

$$\begin{cases} \Delta m = m_2 - m_1 \\ \Delta h = h_2 - h_1 \\ \Delta V = \frac{\Delta m}{\rho} \end{cases} \tag{1}$$

Δm represents the wear quality, where m_2 is the initial mass of the roller, and m_1 is the mass of the roller after completion of the wear test. Δh represents the wear depth, where h_2 is the initial depth of the roller, and h_1 is the depth after the wear test. ΔV represents the wear volume， ρ shows the roller density， the roller density can be obtained from Table S2. The standard deviation S is defined by:

$$S = \sqrt{\frac{\sum_{i=1}^{j}(x_j - \overline{x})^2}{n}} \tag{2}$$

S denotes the sample standard deviation, x_j represents the data for the j_{th} sample, n denotes the number of roller samples, and $\overline{x}$ represents the mean of the samples.

Table S11 gives the comparative results of rim wear volume under different types of rollers and their depth-to-width ratio. Overall, the wear volume of traditional rollers is 230.77 mm^3. Compared with traditional roller, the wear volume of rollers with striped structures is reduced to varying degrees. Among them, the overall performance of arcuate striped rollers is the best. The wear volume ranges under different depth-to-width ratios are about 79.49mm^3-110.26 mm^3, and reaches the lowest value of 79.49mm^3 when the depth-to-width ratio is 0.86; the wear volume of vertical striped rollers is relatively high, ranging from 155.13mm^3-187.18mm^3, but still lower than some operating conditions of traditional rollers; the wear volume of the rhombic striped roller is between 141.03mm^3-175.64 mm^3, which is in the middle. As the depth-to-width ratio changes, there are obvious differences in the wear response of rollers with different structures, indicating that geometric parameters have a significant impact on wear behavior. Among them, the arcuate stripe structure has better comprehensive performance in reducing rim wear. As shown in Table S11, the arcuate stripe roller with optimized depth-width ratio has the lowest wear volume, with a value ranging from 70.51mm^3-76.92mm^3, and the wear resistance is significantly improved. Furthermore, when the depth-width ratio is 0.7750, the wear volume reached the minimum value of 70.51 mm^3.

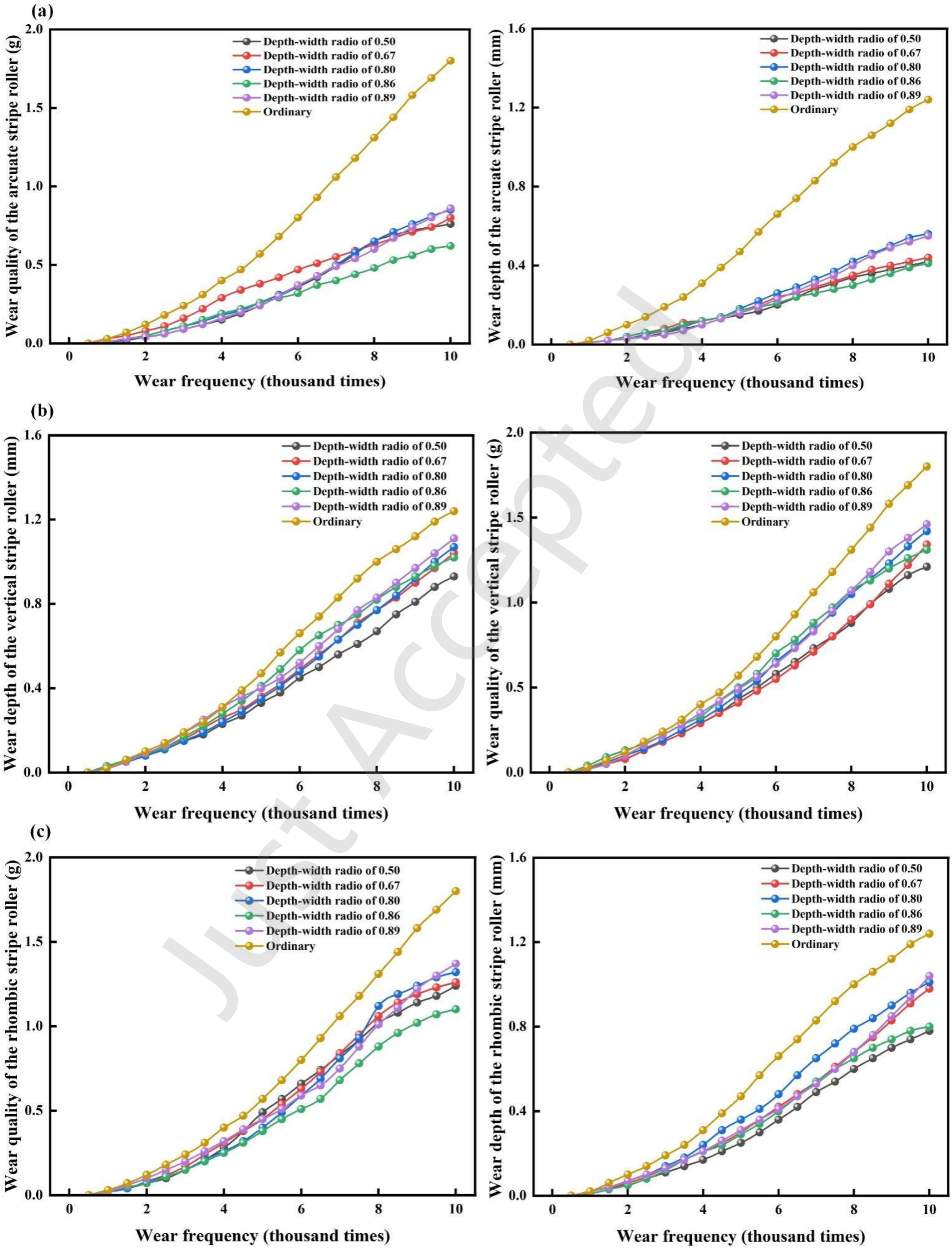

Fig. 4 Evolution of wear mass loss and wear depth of different biomimetic rollers with wear frequency: (a) arcuate stripe

rollers, (b) vertical stripe rollers, and (c) rhombic stripe rollers.

The experimental setup divided roller samples into four groups: rollers with arcuate stripes, rollers with vertical stripes, rollers with rhombic stripes, and ordinary rollers. Comparative experiments were conducted under identical conditions. Each group of rollers underwent 10,000 experimental iterations, with data collected every 500 cycles. Supplementary Materials Tables S3 to S5 present the wear quality and depth data for rollers with arcuate stripes, vertical stripes, and rhombic stripes throughout the experiment. It is worth noting that the ordinary rollers are regarded as the control group.

Upon the completion of the experimental setup for testing the wear resistance of rollers, sixteen roller sets were selected for experimentation. These tests were designed considering the actual operational boundary conditions of the rollers. Subsequent to the data collection and analysis, the arrangements were optimized, leading to the identification of the most effective pattern type and depth-to-width ratio of the rollers.

Based on the results of 10,000-cycle tests on four types of rollers conducted in the reciprocating friction wear experiments, the intrinsic mechanism of surface texture reducing wear and its dependence on the depth-to-width ratio were revealed. The experimental data show that under the same depth-to-width ratio conditions, the arc-shaped stripe rollers exhibit the most excellent anti-wear performance, followed by the rhombic and vertical stripe rollers, and the ordinary rollers perform the worst. This difference stems from the geometric characteristics of the texture: the arc-shaped stripes achieve smooth stress transition through arc-shaped edges, avoiding stress concentration at the straight edges of vertical stripes that causes local peeling; at the same time, their continuous curved groove structure can efficiently capture and retain abrasive particles during the 30 Hz reciprocating motion, effectively inhibiting tri-body abrasive wear. The influence of the depth-to-width ratio is presented in a typical trade-off relationship in all three textures - taking the arc-shaped stripes with the best performance as an example, the wear amount increases with the depth-to-width ratio in the range of 0.5 - 0.80, first decreases and then increases in the range of 0.80 - 0.89, and reaches the lowest point at a depth-to-width ratio of 0.86. At this point, the wear quality and depth are reduced by 65.56% and 66.95% respectively compared to the ordinary rollers, and the standard deviation is the smallest and the stability is the best. This confirms that 0.86 is the optimal balance point: the groove depth is just large enough to accommodate the accumulated abrasive particles, and the raised part does not intensify contact fatigue due to excessive local pressure; too shallow would result in insufficient abrasive capture space, and the abrasive particles would still participate in wear; too deep would cause an increase in the pressure on the raised part, resulting in abrasive rebound. The vertical stripes reach the optimal performance at a depth-to-width ratio of 0.50, with a wear reduction of 32.78% and 25.00%; the rhombic stripes are also optimal at a depth-to-width ratio of 0.86, with a wear reduction of 38.89% and 35.48%, further verifying the universal law that textured surfaces achieve anti-wear enhancement by optimizing abrasive capture ability and stress distribution. These measured data provide reliable friction coefficient input parameters for subsequent simulation analysis.

3.2.3 Surface Characterization of Worn Rollers

In the experimental process, the biomimetic roller engaged in contact interaction with plate components, resulting in relative motion that caused wear. This section explores the wear traces on the roller to assess its wear resistance and anti-wear capabilities. The analysis of the roller's surface morphology post-wear integrates both macroscopic and microscopic perspectives. Supplementary Material Figure S6 presents the macroscopic characterization of 15 sets of three types of biomimetic roller samples post-wear. Fig. 5 depicts the microscopic surface characterization of the worn roller, with the region enclosed in a red frame indicating the area photographed.

As demonstrated in Fig. 5, further analysis of the wear traces on the roller surface was conducted using a confocal microscope, a deep well observation system and a SEM. Fig. 5(a) to 5(d) represent the macroscopic characterization of biomimetic rollers with arcuate, vertical, and rhombic stripes post-wear, observed through SEM and three-dimensional microscopic imaging. It was observed that the surfaces of rollers with arcuate, vertical, and rhombic patterns exhibited dense pit-like pores and elongated grooves. The roller body surface experienced minor material transfers due to the motion of the abrasive particles, whereas the material surface of ordinary rollers underwent more pronounced elongated grooving with significant material transfer. The lower left region of the roller body showed noticeable plastic deformation, indicating severe wear.

The roller body surface of rollers with arcuate stripes was relatively smooth, with a low production of wear debris and no significant depressions, maintaining a smooth surface. The height of the wear marks in the contact area was measured at 60.49 μm. For rollers with vertical stripes, the roller body surface exhibited minor, fine furrow-like and pit-like wear marks due to the movement of wear debris. Frictional motion raised local temperatures, softening the roller body texture and causing plastic deformation, which led to layered spalling. The left side of the roller body appeared darker, with wear mark heights of 76.01 μm. Rollers with rhombic stripes on the right side of the roller body displayed darker regions, with wear mark heights of 65.81 μm. The interaction between wear debris and the roller body under compression resulted in pit-like wear marks and deeper furrow-like grooves. Ordinary rollers exhibited dense pit-like collapses and layered spalling due to friction from wear debris, accompanied by fine wavy furrow-like wear marks and irregular rhombic-shaped depressions. This resulted in a notable material flow on the roller body surface, with wear mark heights reaching 99.40 μm.

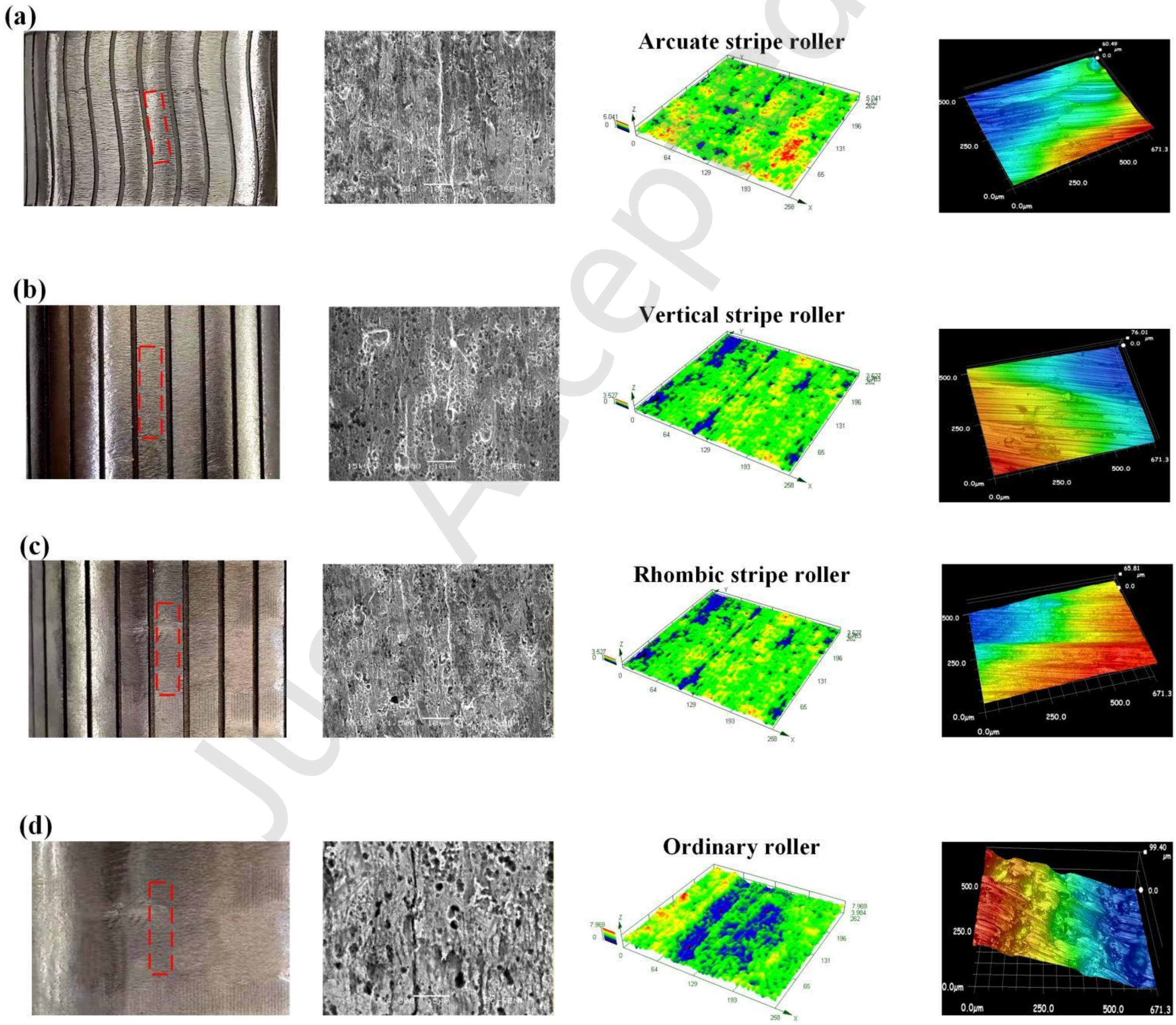

Fig. 5 Wear scar morphologies and three-dimensional surface topographies of different rollers after reciprocating friction tests: (a) arcuate stripe roller, (b) vertical stripe roller, (c) rhombic stripe roller, and (d) ordinary roller.

The formation of the above wear patterns is mainly related to two mechanisms: abrasive wear and adhesive wear. The friction-reducing effect of the textured roller is manifested in its ability to suppress wear by altering the trajectory of the abrasive particles and the distribution of contact stress. For the arc-shaped striated roller, its surface is smooth and there are few abrasive particles because the arc-shaped grooves effectively capture the abrasive particles generated during the friction process, reducing the rolling and sliding of the abrasive particles on the contact interface, thereby inhibiting the occurrence of abrasive wear and maintaining a relatively intact surface. The fine grooves and pit-like traces on the vertical striated roller indicate that some abrasive particles are not completely contained, and they participate in the micro-cutting effect in the contact area to cause abrasive wear; at the same time, the local temperature rise caused by friction heat leads to material softening, and plastic deformation and adhesion occur under the action of alternating stress, thereby causing delamination and shedding, and the darker areas are the material transfer traces formed after the adhesion point is torn. The wear pattern of the rhombic striated roller is between the two, its pits and grooves indicate that the abrasive particles are pressed into the surface under the compressive stress and form pits, and at the same time, they produce a scraping effect due to the movement, but because the texture still has a certain accommodating effect on the abrasive particles, its wear degree is slightly lighter than that of the vertical striated roller. The surface of the ordinary roller has no texture constraint, and the abrasive particles are repeatedly crushed and slid in the contact area, resulting in continuous three-body abrasive wear; at the same time, the accumulation of friction heat intensifies the adhesion and shedding of the material, forming dense peeling pits and irregular depressions, and the wear height significantly increases. In summary, the existence of texture mainly inhibits abrasive wear by accommodating abrasive particles, and reduces adhesive wear by changing the contact state. This is the fundamental reason why the wear patterns of the textured roller are superior to those of the ordinary roller.

By combining the SEM microscopic wear morphology marked in the figure S7, the influence of different depth-to-width ratios and stripe types on the surface damage characteristics of the roller can be systematically compared.

Firstly, regarding the overall influence of depth-to-width ratio: when the depth-to-width ratio is within the range of 0.50 to 0.80, dense micro-crack initiation and expansion traces can be observed on the surfaces of all three types of stripe rollers, indicating that the wear mechanism has shifted from plastic deformation dominance to brittle spalling; when the depth-to-width ratio increases to 0.86, the three types of roller surfaces instead present shallow and wide furrow-like wear marks, with fine and sparse wear debris and only showing mild abrasive scratches; and as the depth-to-width ratio further increases to 0.89, the plastic flow on the surface significantly intensifies, and obvious material accumulation and compression edges appear at the edges of the grooves.

Secondly, comparing the influence of stripe types: for arcuate stripe rollers, they all show slight parallel scratches under various depth-to-width ratios, with consistent wear direction and uniform material removal, and only local layered peeling occurs at depth-to-width ratio of 0.67 and 0.80; for vertical stripe rollers, when the depth-to-width ratio is between 0.50 and 0.80, block-like peeling occurs on the wear surface, presenting typical periodic contact fatigue characteristics, while when the depth-to-width ratio reaches 0.86, only slight parallel scratches are seen on the surface; for rhombic stripe rollers, at an depth-to-width ratio of 0.86, the rhombic grooves can effectively capture wear debris, avoiding secondary scratches, and the surface finish is better than other types of the same scale, but when the depth-to-width ratio is between 0.50 and 0.80, the edges of the grooves undergo adhesive wear and material transfer, accompanied by layered peeling phenomena, and the wear condition is relatively severe.

To evaluate the stability of the arcuate, vertical and rhombic stripe roller surfaces under repeated rolling-sliding contact, SEM scanning electron microscope observations were conducted on the worn roller surfaces. As shown in Fig. 5 and Fig. S7, after the wear test, the overall arcuate, vertical and rhombic geometric structures of the roller surfaces could still be clearly identified. Importantly, no complete collapse or severe flattening of the texture structure was observed. This indicates that, under the current experimental conditions, the arcuate, vertical and rhombic geometric structures of the roller surfaces could still be clearly identified stripes formed by laser processing have sufficient structural stability to withstand long-term friction loads. Therefore, the functional role of the surface texture in regulating contact behavior and improving wear resistance was maintained throughout the entire test period.

3.3 Simulation Analysis

Through stress field simulation, a precise analysis of the regulatory mechanisms of biomimetic textures on the stress distribution at the contact interface was achieved, revealing stress concentration regions and fatigue failure thresholds. This provides a theoretical basis for anti-fatigue optimization of roller structures. Energy analysis, from a thermo-mechanical coupling perspective, quantifies the dynamic balance of friction energy consumption, plastic deformation energy, and thermal energy conversion during the rolling process. Both analyses collaboratively construct a "stress field-energy flow" coupling model, offering theoretical support for the efficient design, process parameter optimization, and reliability assessment of biomimetic rollers.

3.3.1 Maximum Principal Stress Simulation Analysis for Biomimetic Rollers

To further analyze the structural performance of rollers, this subsection explored the stress conditions of biomimetic rollers with three different texture types under static conditions. Using Abaqus software, the rollers were meshed into grid elements, specifically using C3D6RT solid elements. To compute the maximum principal stress that the roller could withstand, the roller body was refined into standard cubic elements. The finite element mesh model of the biomimetic roller is shown in Fig. 6(e). All nodes at the base of the roller body were fixed, constraining the roller's rotational freedom in the X, Y, and Z axes. The contact pressure was set on the roller surface, and the material properties of the roller are detailed in Supplementary File Table S2.

Fig. 6(a)-(c) display the maximum principal stress histograms for biomimetic rollers with depth-to-width ratios of 0.5, 0.67, 0.80, and 0.86 under a pressure of 800N. The results indicate that at a depth-to-width ratio of 0.86, the arcuate, vertical, and rhombic striped rollers achieved optimal maximum principal stresses of 297.7136 MPa, 266.6732 MPa, and 223.4375 MPa, respectively. Under the same depth-to-width ratio conditions, the roller with arcuate stripes exhibited the highest maximum principal stress, followed by the vertical stripes, with the rhombic stripes showing the lowest performance. The maximum principal stresses of the three types of biomimetic rollers were significantly higher than those of ordinary rollers, with stress primarily concentrated on the surface area of the biomimetic ribs, while other areas showed a uniform stress distribution. This indicates that biomimetic textures effectively disperse pressure, significantly enhancing the load-bearing capacity of the rollers. Particularly, the roller with a depth-to-width ratio of 0.86 and arcuate stripes performed optimally, with its maximum principal stress increasing by 191.8136 MPa compared to ordinary rollers, demonstrating the strongest compressive capability. Overall, the load-bearing capacities of all three types of biomimetic rollers were superior to those of ordinary rollers, with the arcuate striped roller exhibiting the best performance at a depth-to-width ratio of 0.86, with a maximum principal stress of 297.7136 MPa.

Moreover, as shown in Fig. 6, the biomimetic texture alters the stress propagation path at the contact interface through periodic geometric constraints, enabling the contact load to be directionally transferred along the primary load-bearing orientation of the texture units. This creates controllable localized stress concentration zones within the surface-reinforced load-bearing elements, while maintaining relatively uniform and low stress levels in the surrounding matrix regions. This load-bearing-element-dominated stress redistribution mechanism essentially corresponds to controlled load localization in structural design, with its core function being to enhance the load-carrying efficiency and stability of the roller. This indicates that the biomimetic texture can effectively redistribute external loads by reconstructing the contact load transfer path, directing them more efficiently into high-stiffness load-bearing areas, thereby reducing ineffective contact energy dissipation and improving the actual load capacity per unit contact area.

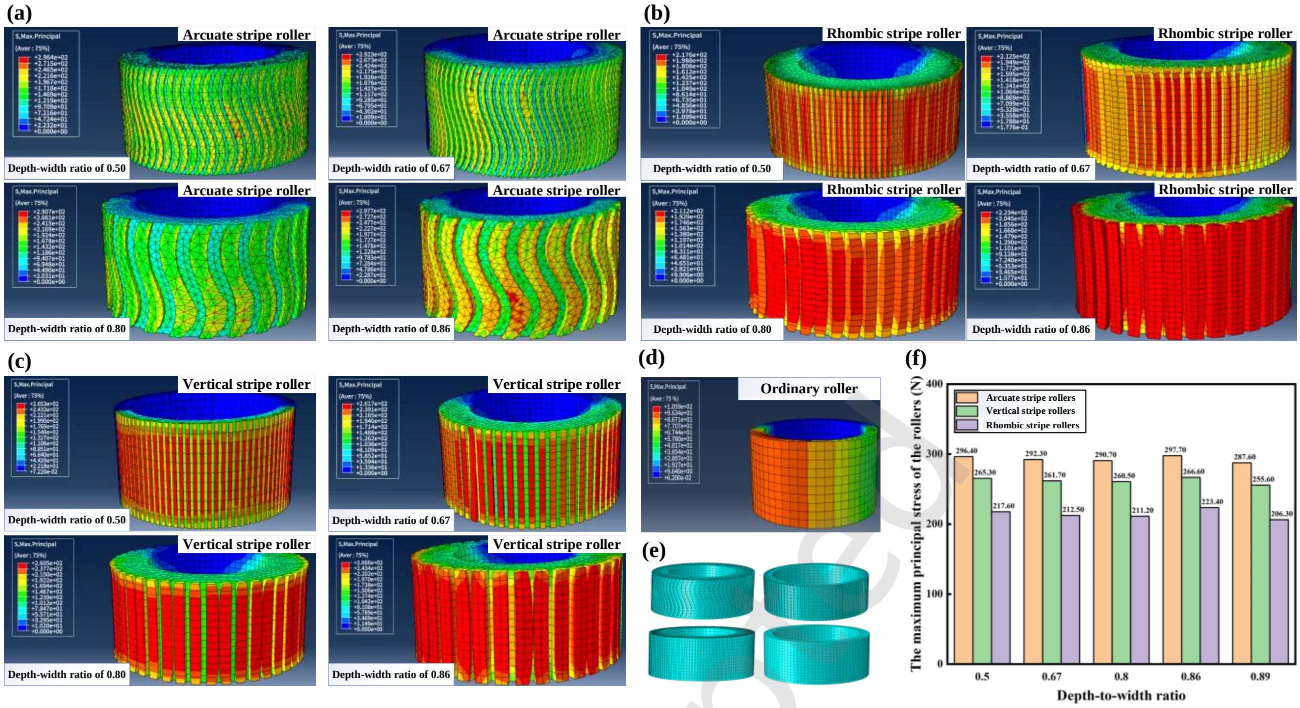

Fig. 6 Finite element analysis of maximum principal stress distributions in biomimetic and ordinary rollers under an 800 N normal load: (a) arcuate stripe rollers, (b) rhombic stripe rollers, (c) vertical stripe rollers, (d) ordinary roller, (e) finite element model, and (f) comparison of maximum principal stresses.

The above simulation results further reveal the mechanism by which biomimetic textures affect the bearing performance of rollers. As shown in Fig. 6(a)-(c), under the same load conditions, the maximum principal stress of the arc-shaped, vertical-shaped, and rhombic-shaped textured rollers is significantly higher than that of the ordinary rollers. Among them, the arc-shaped textured roller with a depth-to-width ratio of 0.86 reaches 297.71 MPa, which is 191.81 MPa higher than that of the ordinary roller. This phenomenon is due to the regulatory effect of the texture structure on the stress distribution: the arc-shaped texture guides the stress to be uniformly transmitted along the texture direction, effectively concentrating the stress at the top of the ribs; the vertical-shaped texture uses the angular structure to form a strengthening zone in the edge area; the rhombic-shaped texture achieves multi-directional dispersion of stress through unit division. The common feature of the three textures is that the stress peak is locked on the surface of the texture ribs, while the stress distribution in the base area tends to be uniform, thereby fully exerting the structural strength of the material.

It is worth noting that although the local stress of the textured rollers is higher, their wear degree is lower than that of the ordinary rollers. This indicates that the relationship between wear and the maximum principal stress is not a simple positive correlation. The capture effect of the texture grooves on the abrasive particles effectively inhibits three-body abrasive wear, causing only slight local wear in the high-stress area; while the ordinary rollers have a lower stress level, but since the abrasive particles cannot be discharged, they continuously participate in the friction process at the contact interface, resulting in large-area material peeling. This result explains why the wear morphology of the textured rollers in Figure 5 is less severe, while the maximum principal stress in Figure 6 is higher, confirming that the biomimetic texture achieves a synergistic improvement in bearing capacity and wear resistance through the dual mechanisms of "stress redistribution" and "abrasive particle control".

3.3.2 Energy Analysis of the Roller in the Friction Process

To analyze the energy dissipation of a biomimetic roller during the rolling process, this section conducts a dynamic analysis of the roller's motion, incorporating boundary conditions encountered during movement. Data extraction was performed to assess the energy losses occurring between the roller and the plate during their interaction. The parameters of the boundary conditions during the roller's movement are detailed in Supplementary Material Table S7.

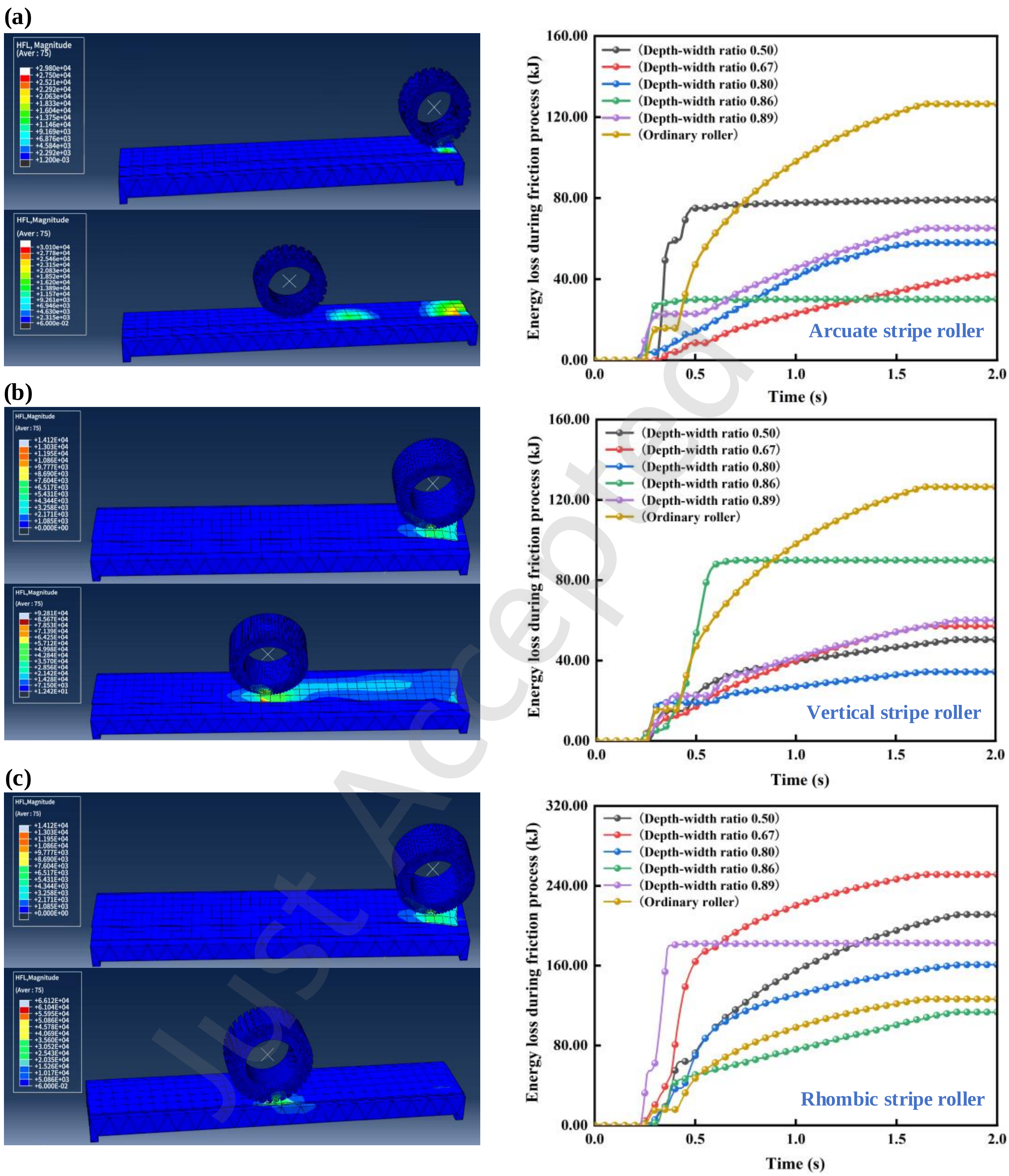

Fig. 7 Frictional energy dissipation distributions and evolution curves of biomimetic rollers with different depth-to-width ratios during rolling contact: (a) arcuate stripe rollers, (b) vertical stripe rollers, and (c) rhombic stripe rollers.

In this study, the HFL module in Abaqus was utilized for contour visualization. The HFL module, representing the energy module, facilitated the analysis of the energy distribution generated through friction between the roller and the plate. The results are depicted in Fig. 8, which illustrates the thermodynamic analysis and energy maps of rollers with arcuate, vertical, and rhombic stripe patterns during the final stage of rolling. The rolling process was divided into 200 frames, with frames 40 and 90 selected for detailed analysis. At frame 40, the roller initially contacts the plate, causing slight plastic deformation at the surface. The energy loss at the contact site of the roller showed an increasing trend with successive rolling actions. By frame 90, the roller had penetrated the surface of the plate and moved smoothly, leading to a stabilization of energy changes. The distribution of energy on the surface of the plate, used in the rolling process, appeared to be superficial.

Supplementary Material Table S8 presents the energy values during the friction process of the roller. Under equivalent depth-to-width ratio conditions, the roller with arcuate stripes exhibited the lowest friction-generated energy, while ordinary rollers showed the highest energy values. Specifically, for rollers with arcuate stripes, the friction energy decreased initially and then increased as the depth-to-width ratio varied between 0.5 and 0.80, reaching 42405.3 J at a depth-to-width ratio of 0.67. Within the depth-to-width ratio range of 0.80 to 0.89, the friction energy demonstrated a similar trend and reached a minimal value of 30072.6 J at a depth-to-width ratio of 0.86.

In the investigation of vertical stripe rollers, it was observed that for depth-to-width ratios ranging from 0.5 to 0.80, the friction energy exhibited an initial increase followed by a decrease. At a depth-to-width ratio of 0.80, the friction energy reached its minimum value of 34358.0 J. Within the depth-to-width ratio interval of 0.80 to 0.89, the friction energy showed a similar trend of initial increase followed by a decrease. In the case of rollers with rhombic stripes, for depth-to-width ratios between 0.5 and 0.86, a similar trend in the friction energy was documented, reaching a minimum value of 113329.0 J at a depth-to-width ratio of 0.86, identifying the depth-to-width ratio of 0.86 as the critical point for minimal friction energy for rollers with rhombic stripes. In the depth-to-width ratio range of 0.86 to 0.89, the wear energy positively correlated with the depth-to-width ratio. Overall, the arcuate stripe rollers demonstrated the lowest friction energy production and optimal thermodynamic performance during a rolling cycle of 0-2 seconds.

To further elucidate the physical meaning of the above frictional energy consumption data, the Fleischer wear model based on energy dissipation is introduced. This model posits that the wear volume V of the material is directly proportional to the energy dissipated W_R during the friction process, and the basic relationship is as follows:

$$V = \frac{W_R}{e_R} \tag{3}$$

In the formula, W_R represents the frictional work, which is the frictional energy consumption output by the Abaqus/HFL module in this paper. e_R is the energy wear coefficient (depending on the material properties, it can be regarded as a constant when the material remains unchanged).

During the simulation process, the friction force is usually handled using the Coulomb friction model, where the friction force f is proportional to the normal contact pressure p:

$$f = \mu p \tag{4}$$

Here, μ represents the friction coefficient. The HFL module of Abaqus calculates the integral of the friction force over the slip distance to obtain the frictional energy consumption E:：

$$E = \int f ds = \int \mu \cdot p ds \tag{5}$$

This energy consumption value directly corresponds to the work done by the friction force in the experiment, thus its magnitude reflects the average friction force level. According to Equation (3), for the same material system, the wear volume is linearly and positively correlated with the friction energy consumption. Based on this, the friction energy consumption values calculated in this paper can reflect the wear trend of the rollers. Moreover, the simulation results show that under the conditions of a depth-to-width ratio of 0.50-0.89, the friction energy consumption of arc-shaped and vertical-striped rollers is significantly lower than that of ordinary rollers. And when the depth-to-width ratio of the arc-striped roller is 0.86, the reduction in friction loss energy reaches 73.74%. According to the Fleischer model, this means that its wear volume will decrease. Therefore, from the perspective of energy dissipation, the optimized biomimetic striped surface, especially the arc-striped one, can significantly reduce the expected wear amount of the rollers during the rolling process, verifying the effectiveness of its wear-resistant design.

3.3.3 Analysis of the wear depth of the biomimetic striped roller during the friction process

To explore the influence of different surface texture structures on the wear performance of rollers, this paper established a bionic roller wear simulation model based on the Abaqus software and used the Archard wear model to numerically simulate the contact wear behavior between the roller and the mating material. In the wear simulation, the roller is used as a deformable body and the metal plate is used as a rigid body. Surface-surface contact is adopted between the two, and rolling-sliding composite contact is formed through the rotation and relative motion of the roller. The wear evolution is based on Archard model of Abaqus, and key variables including contact pressure, friction coefficient, relative sliding distance and sliding speed are all taken into consideration. In order to improving calculation efficiency, the metal plate is set as a rigid body, thus its local elastic-plastic deformation and the resulting change in contact area and stress redistribution are not considered. Since all textured rollers were evaluated under the same load, kinematic and contact conditions, this simplification has little effect on the relative differences in wear resistance. Although the model may affect the quantitative accuracy of the absolute wear amount, it is sufficient to effectively compare the wear resistance of rollers with different surface textures. The total simulation time was 20s, with a focus on analyzing the evolution law of the wear depth of the roller surface stripe structure at different time points. The research objects included three types of bionic stripe rollers - arcuate stripe, rhombic stripe, vertical stripe, as well as a ordinary non-textured roller as a control group. In Figure 8, a1-a4, b1-b4, and c1-c4 represent the wear depth values of the arcuate stripe, rhombic stripe, vertical stripe rollers at a depth-to-width ratio of 0.80 at 5s, 10s, 15s, and 20s, respectively; d1-d4 represent the wear depth values of the ordinary roller at 5s, 10s, 15s, and 20s; e1-e4 represent the wear depth values of the arcuate stripe roller at a depth-to-width ratio of 0.7750 at 5s, 10s, 15s, and 20s, respectively.

As shown in Figure 8 (a1) - (d4), with the increase of simulation time, under the condition of a depth-to-width ratio of 0.80, the wear depth of the three bionic stripe rollers all showed an upward trend, but the wear rate and final wear amount were significantly different. Compared with the ordinary roller, the wear depth of the three bionic stripe rollers at the same time points was all lower, indicating that the surface stripe structure helps to improve the stress distribution in the contact area and delay the wear process. Among them, the arcuate stripe roller had the smallest wear depth at each time point, showing the best wear resistance performance; while the wear depth of the vertical stripe roller was relatively low, and the wear depth of the rhombic stripe roller was higher, but still better than that of the ordinary roller.

As shown in Figure 8 (e), by comparing the wear curves of the arcuate stripe roller under depth-to-width ratios of 0.80 and 0.775, it can be found that the change in the depth-to-width ratio has a significant impact on the wear depth. When the depth-to-width ratio was optimized to 0.775 by the golden section method, the wear depth of the roller at each time points increased, indicating that an appropriate depth-to-width ratio setting is of great significance for optimizing the wear resistance performance of bionic rollers.

In conclusion, Figure 8 visually demonstrates the influence laws of different bionic stripe structures and their geometric parameters on the wear process of rollers, providing a reference basis for the structural optimization design of bionic wear-resistant rollers.

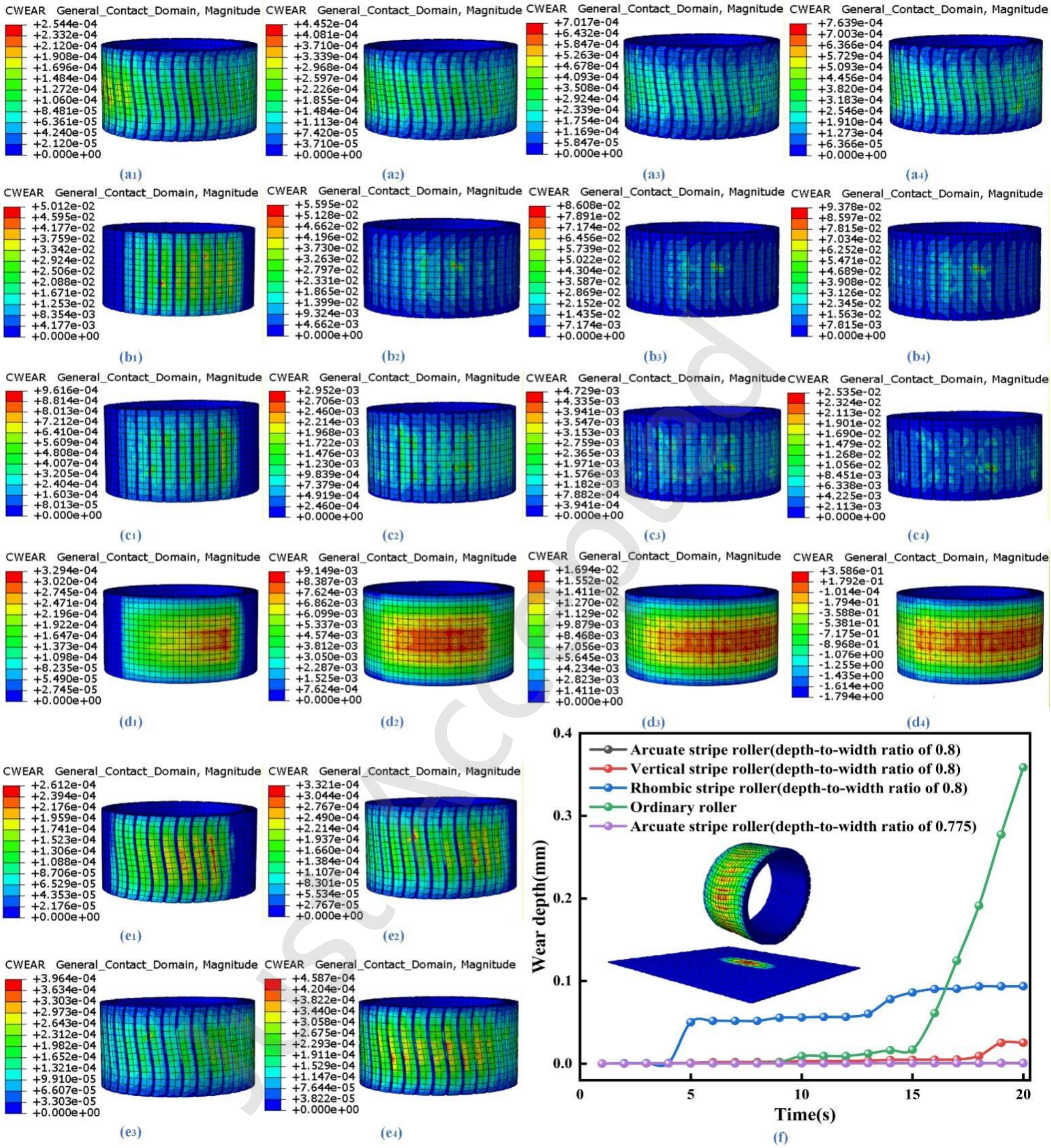

Fig.8 Finite element simulation of wear evolution in different rollers. (a) wear depth distributions of arcuate stripe rollers with a depth-to-width ratio of 0.80, (b) wear depth distributions of vertical stripe rollers with a depth-to-width ratio of 0.80, (c) wear depth distributions of rhombic stripe rollers with a depth-to-width ratio of 0.80, (d) wear depth distributions of ordinary rollers, and (e) wear depth distributions of optimized arcuate stripe rollers with a depth-to-width ratio of 0.775 (f) wear depth evolution of arcuate, vertical, rhombic stripe rollers and the ordinary roller during the wear cycle from 0 to 20 s.

3.4 Optimization of depth-to-width Ratio in Biomimetic Rollers

To clarify the performance evolution patterns under different depth-to-width ratios, this study adopts a phased optimization strategy of discrete parameter screening—continuous interval optimization. First, multiple discrete parameter points within the 0-1 depth-to-width ratio range, such as 0.50, 0.67, 0.80, 0.86, and 0.89 are selected to conduct single-factor comparative analyses on arcuate, vertical, and rhombic grooved rollers, aiming to evaluate the effects of various groove profiles and depth-to-width ratios on the mechanical and tribological properties of the rollers. The results indicate that under discrete parameter conditions, the arcuate stripe roller exhibits the best overall performance. Among these, a depth-to-width ratio of 0.86 demonstrates optimal comprehensive performance in terms of load capacity, friction energy, and wear resistance, thus being identified as the local optimum solution.

To further improve the accuracy of parameter optimization, this study introduces the golden section method for the arcuate stripe roller to precisely search the continuous depth-to-width ratio space. Since stress, friction energy, and wear indicators exhibit continuous and unimodal response characteristics with respect to the depth-to-width ratio, the golden section method effectively enables rapid convergence toward the optimal parameters. Ultimately, a depth-to-width ratio of 0.775 is identified as the global optimum under continuous optimization conditions, whose overall performance further surpasses the local optima obtained under discrete parameter settings.

The Golden Section method [45], widely employed by researchers in aeronautics, apparel, mathematics, and engineering manufacturing, was utilized in this section to iteratively calculate the optimal depth-to-width ratio for arcuate stripe rollers. Structural performance of the optimized roller was subsequently validated through simulation analysis.

Based on the conclusions drawn from simulation and experiments research, the optimum depth-to-width ratio range for the arcuate striated roller was determined to be between 0.5 and 0.86. Employing the principles of the golden ratio, combined with the actual dimensions of the biomimetic roller, values of a = 0.50 and b = 0.86 were selected and subsequently incorporated into the proportion calculation formula as shown in Equation (6).

$$\begin{cases} r = a + 0.382(b - a) \\ u = a + 0.618(b - a) \end{cases} \tag{6}$$

Through iterative calculations, four sets of depth-to-width ratio proportions were derived, with the iterations totaling four. The optimized texture parameters post-depth-to-width ratio optimization are detailed in Supplementary Material Table S9. To further discuss the performance of the roller following depth-to-width ratio optimization, this section conducts a static simulation and dynamic analysis of the arcuate striated roller with optimized depth-to-width ratios.

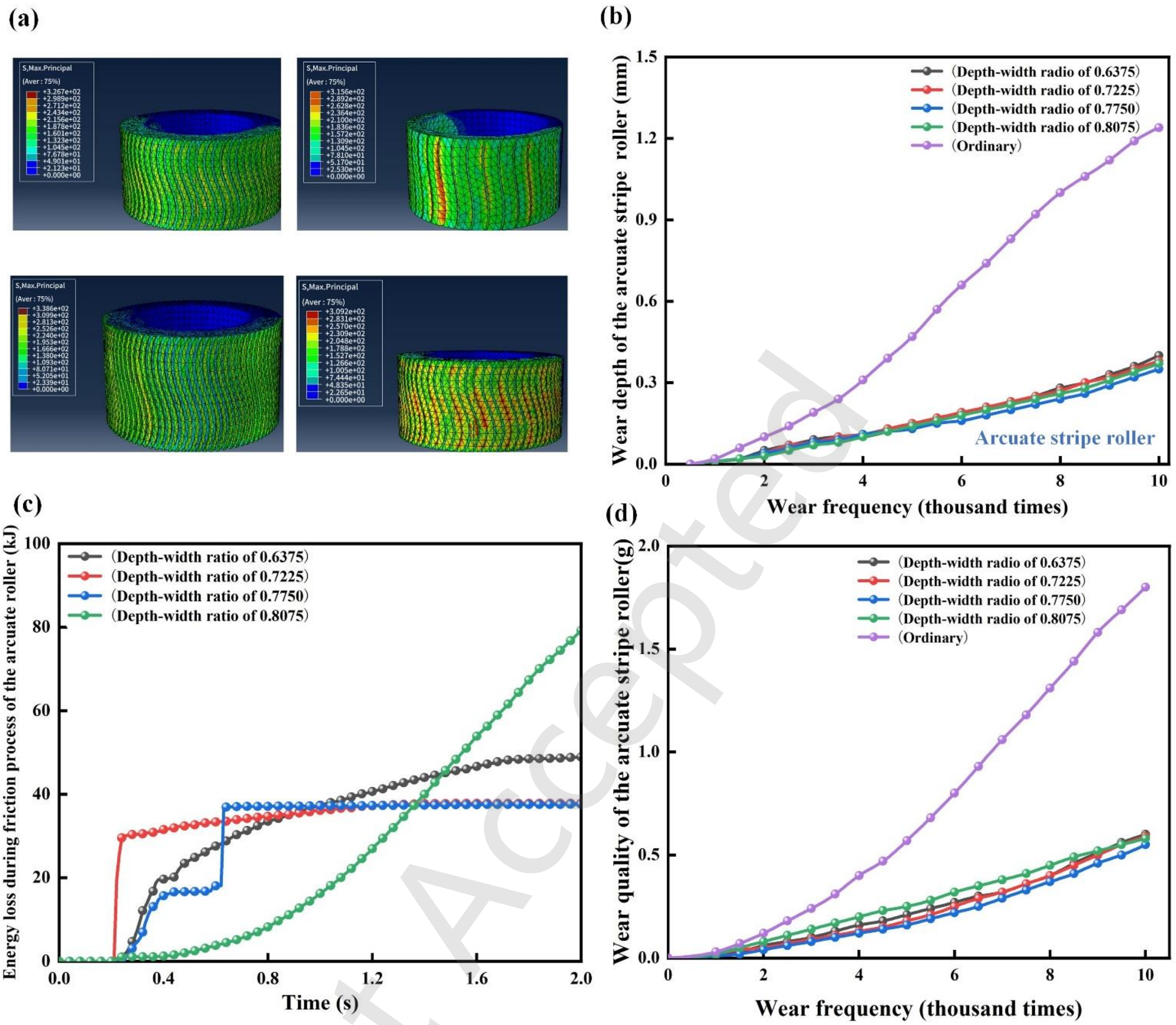

Fig. 9 Performance evaluation of optimized arcuate stripe rollers with different depth-to-width ratios: (a) maximum principal stress distributions, (b) wear depth, (c) energy loss during friction process(d) wear quality.

As evident from Fig. 9(a), under a surface load of 800N, the maximum principal stress that the arcuate striated roller (with a depth-to-width ratio of 0.7750) can withstand is 338.6 MPa, which is the highest among the four sets. The maximum principal stresses that the other three biomimetic rollers can withstand show a significant decrease. Thus, it can be inferred that the depth-to-width ratio optimized via the golden ratio method enhances resistance to external loads, thereby improving wear resistance. From Fig. 9(c), it is observed that when the depth-to-width ratio of the arcuate stripe roller is 0.7750, the maximum energy generated due to rolling friction is the lowest at 27490.88 J, which represents a reduction of 98960.12 J compared to a ordinary roller. The texture structure optimized using the golden ratio method significantly disperses the load distribution across the roller surface, enhances load-bearing capacity and structural stability, and reduces energy generated from rolling friction, thereby significantly improving thermodynamic performance.

Analysis of Supplementary Material Table S10 and Fig. 9(b) and (d) reveals that the wear quality and wear depth of the arcuate striated roller with a depth-to-width ratio of 0.6375 are respectively 1.20 g and 0.84 mm lower than those of an ordinary roller. Similarly, for the arcuate striated roller with a depth-to-width ratio of 0.7225, the wear quality and wear depth are respectively 1.21 g and 0.86 mm lower than those of an ordinary roller. For the roller with a depth-to-width ratio of 0.7750, the reductions in wear quality and wear depth are the greatest, at 1.25 g and 0.89 mm respectively, thus indicating optimal wear resistance and anti-wear capabilities.

4. Conclusion

This study thoroughly investigates the anti-friction and wear-resistant mechanisms of the non-smooth surface of pearl shells, and applies biomimetic theory to the structural design of rollers to enhance its wear resistance and anti-wear performance. The main research is concluded as follows:

1.Inspired by the non-smooth surface structure of pearl shells, three biomimetic striped rollers—arcuate, vertical, and rhombic-shaped were designed. Static analysis showed that under an 800N load, the arcuate roller exhibited the best load-bearing capacity among the three structures, with a maximum principal stress reaching 297.71MPa and optimal structural stability.

2.In the single-factor comparative analysis of bionic stripe patterns and depth-to-width ratio parameters, a comparison of different depth-to-width ratios revealed that the arcuate stripe roller exhibited the best overall performance in terms of stress distribution, friction energy, and wear resistance. Moreover, its comprehensive performance reached a local optimum when the depth-to-width ratio was 0.86.

3.Based on identifying the arcuate groove roller as the optimal texture type, the depth-to-width ratio of the arcuate groove roller was further optimized using the golden section method, resulting in a globally optimal depth-to-width ratio of 0.7750. At this depth-to-width ratio, the arcuate groove roller achieves global optimum performance in both load-carrying capacity and thermal-friction characteristics. The energy generated by rolling friction is reduced to 27490.88 J compared to ordinary rollers, demonstrating superior anti-wear performance.

4.The simulation results of wear depth further confirmed the experimental findings, indicating that within a 20 seconds simulation period, the wear depth of arcuate, vertical, and rhombic-shaped roller patterns was lower than that of ordinary rollers. Additionally, the globally optimal depth-to-width ratio for the arcuate roller optimized using the golden section method was determined to be 0.775, achieving the best wear resistance performance.

In summary, the overall performance of the arcuate texture roller is significantly superior to that of vertical, rhombic, and ordinary rollers. Further optimization of its depth-to-width ratio revealed that a value of 0.775 achieves global optimal performance, with peak performance in load capacity, frictional energy loss, and wear resistance.

Statement of originality

We hereby declare that the work submitted for consideration, titled "Design of Pearl Shell-Inspired Biomimetic Textured Rollers and Their Tribological Performance during Roller Hemming", is original and has not been published elsewhere, nor is it under consideration for publication elsewhere. We have no conflict of interest, and the manuscript has been read and approved for submission by all the authors.

Declaration of Competing Interest

The authors declare that they have no known competing financial interests or personal relationships that could have appeared to influence the work reported in this paper.

Acknowledgements

The authors are grateful to Hongwei Zhao，Changyi Liu, Ziqiang Zhang, and Bangcheng Zhang for their help in testing and surface analysis. The study is partially supported by the Jilin Provincial Science and Technology Department, P. R. China (SKL202302016), the National Major Scientific Research Instrument Development Project (52227810), the National Key R&D Program of China (2022YFA1604000), the National Natural Science Foundation of China under Grant (52205565) the National Natural Science Foundation of China under Grant (52275006), the Science Fund for Creative Research Groups of the National Natural Science Foundation of China (52021003), ,the Jilin Provincial Natural Science Foundation under Grant

(20240101134JC).

Data availability

The data that support the findings of this study are available from the corresponding author upon reasonable request.

References

[1] Guinea, A., Aginagalde, A., Tato, W. et al. Impact of surface roughness on the coefficient of friction of polymer-on-polymer contacts for deflection pulley-rope systems in the lift industry. Friction 12, 2126–2138 (2024). https://doi.org/10.1007/s40544-024-0881-8.

[2] Shrestha, S., Spiryagin, M., Bernal, E. et al. Recent advances in wheel-rail RCF and wear testing. Friction 11, 2181–2203 (2023). https://doi.org/10.1007/s40544-022-0705-7.

[3] Yin H , Yang J , Gu Q . Numerical study on the hydrodynamic lubrication performance improvement of bio-inspired peregrine falcon wing-shaped microtexture[J]. Tribology International, 2024, 191(000):18. DOI:10.1016/j.triboint.2023.109049.

[4] Ma J , Liu Y , Yi P ,et al. Anti-friction mechanism of sinusoidal texture with various intervals: The synergistic effect of dynamic pressure and tribofilm[J]. Tribology International, 2022:173. DOI:10.1016/j.triboint.2022.107635.

[5] Cheng, HR., Shin, KH. & Kim, H.S. Enhancement of mechanical and tribological performance of Ti–6Al–4V alloy by laser surface alloying with Inconel 625 and SiC precursor materials. Friction 12, 2089–2107 (2024). https://doi.org/10.1007/s40544-024-0878-3.

[6] Zhao X , Zhang Y , Gao S . Analysis and evaluation of the synergistic effect of ceramic materials and surface texture on anti-abrasive particle wear under rolling conditions[J]. Tribology International, 2024, 197(000):31. DOI:10.1016/j.triboint.2024.109821.

[7] Badler, D., Kligerman, Y. & Kasem, H. Attachment ability of combined biomimetic adhesive micro-textures of different shapes. Friction 11, 1430–1441 (2023). https://doi.org/10.1007/s40544-022-0675-9.

[8] Huang, Q., Wu, C., Shi, X. et al. Topology optimization of AISI 4140 steel with surface texture filled by multi-solid lubricants for enhancing tribological properties. Friction 12, 2033–2051 (2024). https://doi.org/10.1007/s40544-024-0863-x.

[9] Zhang, S., Bai, P., Wen, X. et al. Effects of surface morphology on tribological properties of Arapaima gigas scales. Friction 12, 1469–1482 (2024). https://doi.org/10.1007/s40544-023-0806-y.

[10] Song, X., Hou, Z., Gan, Z. et al. Biomimetic lubricant-grafted surfaces on laser-textured microwell arrays with multifunctionality. Friction 12, 2707–2725 (2024). https://doi.org/10.1007/s40544-024-0906-3.

[11] Yang H , Yang X , Cong J ,et al. Wear behavior of microgroove texture of cemented carbide tool prepared by laser surface texture[J]. Microfluidics and nanofluidics, 2023. DOI:10.1007/s10404-023-02650-7.

[12] Zheng G , Lin Y . Tribological Properties of Micro-Groove Cemented Carbide by Laser Processing. [J]. Micromachines, 2021, 12(5). DOI:10.3390/mi12050486.

[13] Wu, C., Yang, K., Ni, J. et al. Investigations for vibration and friction torque behaviors of thrust ball bearing with self-driven textured guiding surface. Friction 11, 894–910 (2023). https://doi.org/10.1007/s40544-022-0627-4.

[14] Liu S , Sai Q , Wang S ,et al. Effects of Laser Surface Texturing and Lubrication on the Vibrational and Tribological Performance of Sliding Contact[J]. Lubricants, 2022. DOI:10.3390/lubricants10010010.

[15] Yang, W., Wang, J., Wang, X. et al. Anisotropic tribology and electrification properties of sliding-mode triboelectric nanogenerator with groove textures. Friction 12, 1828–1837 (2024). https://doi.org/10.1007/s40544-024-0861-z.

[16] Guo J , Hu T , Li Q ,et al. Nanosecond laser-induced dimple texturing of TB6 alloy surfaces: Tribological behavior under dry and starved-oil lubrication[J].Tribology International, 2024, 197. DOI:10.1016/j.triboint.2024.109842.

[17] Guo J , Wang F , Liou J J ,et al. Tribological properties of picosecond laser-textured titanium alloys under different lubrication conditions[J].Ukrainian journal of physical optics, 2022.

[18] Chen J , Zeng L , Wan Q ,et al. Effects of texture geometry on the tribological performance of brass with a TiN coating under lubricated rotation[J]. AIP Advances, 2019(10).DOI:10.1063/1.5124449.

[19] Qiu Y , Khonsari M M . Experimental investigation of tribological performance of laser textured stainless steel rings[J]. Tribology International, 2011, 44(5):635-644. DOI:10.1016/j.triboint.2011.01.003.

[20] Wang X , Kato K , Adachi K ,et al. Loads carrying capacity map for the surface texture design of SiC thrust bearing sliding in water[J]. Tribology International, 2003, 36(3):189-197. DOI:10.1016/S0301-679X(02)00145-7.

[21] Cui Z , Guo Z , Yuan C . Influence of different rhombic surface textures on the tribological performance of water-lubricated bearings[J]. Materials Express, 2020, 10(9):1452-1462.DOI:10.1166/mex.2020.1761.

[22] Quan S , Yong G , Jun G ,et al. Effect of fish scale texture on friction performance for reciprocating pair with high velocity[J]. Industrial Lubrication and Tribology, 2019, ahead-of-print(ahead-of-print). DOI:10.1108/ILT-09-2019-0398.
[23] Tong J, Zhang Q Z, Chen D H, et al. Effects of bionic geometric structure press rollers on reducing rolling resistance and adhesion against soil[J]. Applied Mechanics and Materials, 2014, 461: 63-72.
[24] Zhao C , Long R , Zhang Y ,et al. Influence of characteristic parameters on the tribological properties of vein-bionic textured cylindrical roller thrust bearings[J]. Tribology International, 2022.
[25] Johannes, Schneider, Vergil ,et al. Friction reduction through biologically inspired scale-like laser surface textures.[J]. Beilstein Journal of Nanotechnology, 2018. DOI:10.3762/bjnano.9.238.
[26] Ferreira, R., Carvalho, Ó., Sobral, L. et al. Laser texturing of piston ring for tribological performance improvement. Friction 11, 1895–1905 (2023). https://doi.org/10.1007/s40544-022-0723-5.
[27] Ziqiang Zhang, Junye Li, Tiangang Zou, et al. Effect of nozzle arrangement on heat dissipation performance and mechanical efficiency loss of bionic texture gear [J]. Surface Topography: Metrology and Properties,2024,12(3):1-33.
[28] Xiong D , Qin Y , Li J ,et al. Tribological properties of PTFE/laser surface textured stainless steel under starved oil lubrication[J]. Tribology International, 2015, 82:305-310.DOI:10.1016/j.triboint.2014.07.017.
[29] P. V B , Syed I , Beera S B .Influence of positive texturing on friction and wear properties of piston ring-cylinder liner tribo pair under lubricated conditions[J].Industrial Lubrication & Tribology, 2019.DOI:10.1108/ILT-07-2017-0203.
[30] Arslan A , Masjuki H H , Varman M ,et al. Effects of texture diameter and depth on the tribological performance of DLC coating under lubricated sliding condition[J].Applied Surface Science, 2015, 356(NOV.30):1135-1149. DOI:10.1016/j.apsusc.2015.08.194.
[31] Kovalchenko A , Ajayi O , Erdemir A ,et al. Friction and wear behavior of laser textured surface under lubricated initial point contact[J].Wear, 2011, 271(9-10):1719-1725.DOI:10.1016/j.wear.2010.12.049.
[32] Uehara Y , Nanbu T , Koiduka Y ,et al. Friction Reduction Using Micro Texture on Inner Type 2 Roller Test and Reciprocal Type Test[J]. Journal of the Japan Society for Precision Engineering, 2016, 82(3):278-284.DOI:10.2493/jjspe.82.278.
[33] Wakuda M , Yamauchi Y , Kanzaki S ,et al. Effect of surface texturing on friction reduction between ceramic and steel materials under lubricated sliding contact[J]. Wear, 2003, 254(3-4):356-363.DOI:10.1016/S0043-1648(03)00004-8.
[34] Chilamakuri S , Bhushan B . Effect of peak radius on design of W-type donut shaped laser textured surface[J]. Wear: an International Journal on the Science and Technology of Friction, Lubrication and Wear, 1999(2):230.
[35] Duoji R , Luo S , Chang X . Study on Hydrodynamic Lubrication and Friction Reduction Performance of Cylindrical Rolls With Tesla Valve Texture[J]. Tribology Transactions, 2023, 66(6):981-991.DOI:10.1080/10402004.2023.2249955.
[36] P., Anand, P., Ramkumar, K. P., Lijesh, Edachery, Vimal, Tribological Performance of Laser-Based Surface Textured Nonconformal Contacts, Advances in Tribology, 2024, 1424767, 25 pages, 2024. https://doi.org/10.1155/2024/1424767
[37] Mourier L, Mazuyer D, Ninove F, Lubrecht AA. Lubrication mechanisms with laser-surface-textured surfaces in elastohydrodynamic regime. Proceedings of the Institution of Mechanical Engineers, Part J: Journal of Engineering Tribology. 2010;224(8):697-711. doi:10.1243/13506501JET771
[38] Zhou, R. S. (1993). Surface Topography and Fatigue Life of Rolling Contact Bearing. Tribology Transactions, 36(3), 329 – 340. https://doi.org/10.1080/10402009308983167
[39] Greco, A., Martini, A., Liu, Y., Lin, C., & Wang, Q. J. (2010). Rolling Contact Fatigue Performance of Vibro-Mechanical Textured Surfaces. Tribology Transactions, 53(4), 610 – 620. https://doi.org/10.1080/10402000903518861
[40] 10. Gimeno S, Mescheder H, Quintana I, et al. Effect of different laser texturing patterns on rolling contact surface and its tribological & fatigue life behavior on 100Cr6 bearing steel, [J]. Wear, 2023, 522: 204717. DOI: 10.1016/j.wear.2023.204717
[41] Zhang B C , Zhang Z Q , Sun J W ,et al.Design and wear resistance analysis of bionic roller for folding of automobile body cover parts based on pearl shell surface texture[J].Surface Topography: Metrology and Properties, 2020, 8(4):045027 (18pp).DOI:10.1088/2051-672X/abce0e.
[42] Oaki Y ,Prof. I H .The Hierarchical Architecture of Nacre and Its Mimetic Material[J].Angewandte Chemie,2005,117(40):6729-6733.DOI:10.1002/ange.200500338.
[43] Sun, J., Guo, W. Chemical-mechanical stability of the hierarchical structure of shell nacre. Sci. China Phys. Mech. Astron. 53, 380–388 (2010). https://doi.org/10.1007/s11433-010-0134-x.
[44] Jiyu Sun, Bharat Bhushan; Hierarchical structure and mechanical properties of nacre: a review. RSC Adv. 2012; 2 (20): 7617–7632. https://doi.org/10.1039/c2ra20218b.
[45] J, Alikhani, Koupaei, et al. A new optimization algorithm based on chaotic maps and golden section search method[J]. Engineering Applications of Artificial Intelligence, 2016, 50:201-214.